Spatial Non-stationary Near-field Channel Modeling and Validation for Massive MIMO Systems

Yuan, Zhiqiang; Zhang , Jianhua; Ji, Yilin; Pedersen, Gert Frølund; Fan, Wei

Published in:
I E E E Transactions on Antennas and Propagation

Publication date:
2022

Spatial Non-stationary Near-field Channel Modeling and Validation for Massive MIMO Systems

Zhiqiang Yuan, Jianhua Zhang, Yilin Ji, Gert F. Pedersen, and Wei Fan

***Abstract*—Massive MIMO is envisioned as a promising technology in 5G and beyond 5G communication. Channel models are of great importance for the development and performance assessment of massive MIMO systems. Since massive MIMO systems are equipped with large-aperture antenna arrays, antenna elements at different spatial positions would observe different channel multipath characteristics, which is so-called spatial non-stationarity (SnS). The SnS property of multipaths has been observed in many reported massive MIMO channel measurements. However, characterization and explanations of SnS have not been adequate in existing statistical channel modeling, and deterministic models (e.g., Ray-tracing) are difficult to implement due to the high complexity. This paper proposes a realistic yet low-complexity SnS channel modeling framework for massive MIMO systems and its validation based on both channel measurements and Ray-tracing simulations. In this work, we firstly perform an 6 GHz-bandwidth millimeter-wave (mmWave) indoor channel measurement campaign with a 0.5 m-radius virtual uniform circular array (UCA), where the SnS phenomena are clearly observed. Then, we propose the massive MIMO channel modeling framework that captures the observed SnS property from physical propagation mechanisms of dominant multipaths in mmWave channels, i.e., blockage, reflection, and diffraction. Compared to traditional stationary channel modeling, only one extra parameter accounting for SnS has been added in the proposed framework, which is desirable for its low-complexity implementation. Finally, the proposed framework is validated with site-specific Ray-tracing simulations. The SnS phenomena observed in the measurements are reproduced well in the modeling results according to the proposed framework, and high similarities between the target channels and modeling results are achieved. The proposed framework is valuable for the development of massive MIMO systems, since it is realistic, low-complexity, and accurate.**

***Index Terms*—Massive MIMO channel measurements and modeling, spatial non-stationarity, Ray-tracing, visibility region, millimeter-wave channel sounding.**

I. Introduction

Massive MIMO has been envisioned as a promising technology to realize the explosive data demand in 5G and beyond 5G communication [1]. Compared to traditional MIMO technologies, the number of antenna elements will be further increased by an order of magnitude in massive MIMO systems (typically, tens to thousands) [2]. With such a large-scale array deployed at base stations (BSs), massive MIMO technologies can provide significant improvement in system performance from aspects of spectral efficiency, capacity, and reliability [3]–[5]. Hence, the development of massive MIMO systems has gained huge attention from both academia and industry [2].

Accurate, realistic, yet easy to utilize channel models are essential for the development of massive MIMO systems [6]–[9]. Several massive MIMO channel sounding campaigns were reported in the literature for building such realistic channel models. In [10], [11], outdoor channel measurements at 2.6 GHz were performed with two 128-element antenna arrays. In [12], [13], indoor measurements with 720- and 360-element virtual uniform circular arrays (UCAs) were conducted at millimeter-wave (mmWave) bands. Several massive MIMO channel measurements were performed in [14]–[18], where space-alternating generalized expectation-maximization (SAGE) algorithms were applied for multipath parameter extraction. Based on those measurements, it was concluded that two assumptions applied for traditional MIMO systems might be violated in massive MIMO systems. First, the far-field assumption might be violated in typical massive MIMO deployment scenarios since the resulting Fraunhofer distance (i.e., $2D^2/\lambda$, with D and λ denoting the antenna aperture and wavelength, respectively) might exceed the distance between the base station and the user [19]. Secondly, spatial non-stationarity (SnS) phenomena might arise in massive MIMO systems, where different spatial channels can be observed by different antenna elements in the massive MIMO array. It is due to the fact that objects with limited sizes in the propagation environment might no longer serve as complete scatterers for the entire array with such a large aperture. Therefore, unlike previous MIMO systems, the near-field effect and SnS characteristic are new challenges introduced in massive MIMO scenarios, which must be considered in realistic channel modeling [20]. The problem will become more pronounced for future ultra-massive MIMO systems, which is considered as a key technology for beyond 5G communication [21].

In the literature, there exist many research works on massive MIMO channel modeling with the near-field effect considered. Regarding standardized channel models, such as the latest 3GPP model TR 38.901 [22], it is recommended to use spherical-wave propagation to characterize near-field channels, where signals are assumed to be radiated from point sources with spherical wavefront. On the contrary, few models have taken the SnS property into consideration [23]. In the context of deterministic channel modeling, the METIS project [24] proposed a Ray-tracing based model for massive MIMO channels, where SnS can be characterized due to the site-specific property of Ray-tracing. However, the high calculation

Zhiqiang Yuan and Jianhua Zhang are with State Key Lab of Networking and Switching Technology, Beijing University of Posts and Telecommunications, China (email: {yuanzhiqiang, jhzhang}@bupt.edu.cn).

Yilin Ji, Gert F. Pedersen, and Wei Fan are with the antennas, propagation, and millimeter-wave systems (APMS) section, the Department of Electronic Systems, Aalborg University, Denmark (email:{yilin, gfp, wfa}@es.aau.dk).

complexity and lack of detailed digital maps and material databases make this approach less attractive. In the context of statistical channel modeling, the COST 2100 model [25] first proposed the concept of visibility region (VR) to characterize SnS channels for MIMO antennas. It confines the cluster activity within a limited geographical area for mobile stations. In [26], the concept of VR was further extended to massive MIMO antenna arrays. Specifically, only antenna elements in VR can *see* the cluster while those out of VR can not. Besides, visibility gain was introduced to capture the distance-dependent variation of the cluster power over elements in VR. Based on the concept of VR, the birth-death process in array axis was utilized in [27]–[30] to statistically characterize the SnS property. Numerical analysis of statistical properties, such as correlation, the quasi-stationarity region, and average cluster life periods on elements, was performed for model validation. In [16], [31]–[33], VR-based massive MIMO channel models were proposed for various scenarios, e.g., indoor and outdoor. Statistic characteristics, such as delay spread, angular spread, and K factor, were compared between the measured channels and modeling results for validation.

Although efforts have been made to characterize massive MIMO channels, most existing VR-based channel modeling frameworks fail to realistically capture and explain the SnS observations. For instance, the significant path power change across visible elements, which is observed in our measurements (see Section II-B), is not well characterized in the state-of-the-art works on SnS. The VR concept would fail to capture the power change since only relatively low spherical power variation among visible elements is assumed in VR-based models [26]. More importantly, explanations of those SnS experimental phenomena, which are crucial for realistic channel modeling, have not been adequate in the literature. Secondly, to the authors' best knowledge, validation of the modeling framework with both channel measurements and Ray-tracing simulations is still missing. Compared to statistical parameters or numerical analysis for validation in the literature, those practical channel data is more reliable and helpful to explain the SnS characteristic in the validation. Moreover, current massive MIMO channel modeling is highly complicated as demonstrated in [34], which makes it difficult to use in practice.

To fill the above gaps, a realistic yet low-complexity SnS channel modeling framework is proposed and validated based on massive MIMO channel measurements and Ray-tracing simulations in this paper. The contributions of this paper are summarized as follows:

- A millimeter-wave (mmWave) channel measurement campaign covering the frequency band from 26.5 to 32.5 GHz with a large-scale virtual UCA (with a radius of 0.5 m and 720 elements) is performed. Thanks to the high resolution in the delay domain and the introduction of metallic boards for blockage, the SnS phenomena of multipath trajectories on such a large array are clearly observed. It provides the measurement database to accurately capture the SnS characteristic.
- A realistic massive MIMO channel modeling framework is proposed, where the observed SnS property is characterized from the propagation mechanism viewpoint of dominant multipaths in mmWave channels, i.e., blockage, reflection, and diffraction. Compared to traditional near-field stationary models, only one additional SnS parameter is newly introduced, resulting in the low-complexity implementation of the proposed framework.
- Ray-tracing simulations with same configurations as the measurements are conducted to provide multipath parameters for the framework validation. The Ray-tracing simulations are demonstrated to accurately predict the measurement results. The SnS phenomena observed in both the measurements and Ray-tracing simulations are captured well by the proposed modeling framework. Furthermore, the proposed framework accurately reproduces the target SnS channels from Ray-tracing simulations, yet with much reduced complexity.

In Section II, ultra-wideband[1] large-scale channel measurements are detailed. Based on the SnS observations from measured data, a novel massive MIMO channel modeling framework revealing the SnS characteristic is proposed in Section III. In Section IV, the framework is validated based on Ray-tracing simulations. Finally, Section V concludes the work.

II. Channel Measurements and SnS Observations

This section presents an indoor channel measurement campaign with the deployment of ultra-wide bandwidth and the large-scale antenna array. A line-of-sight (LoS) scenario and two obstructed-LoS (OLoS) scenarios with the LoS path obstructed by metallic obstacles of different sizes were measured. The metallic boards are intentionally induced to generate the SnS phenomena on the LoS path. From measurement results, the SnS characteristic of channel multipaths can be clearly observed, and the preliminary investigation is presented.

A. Measurement Description

The measurements are conducted in an indoor room of dimensions 4.78×8.19 m^2, in Aalborg University, Denmark, as shown in Fig. 1. The scenario sketch, including the size, location, and material of the objects in the room, is detailed in Fig. 1, and the measurement specifications are presented in Table I. Two omni-directional biconical antennas [36] [37] are exploited as the transmitter (Tx) and receiver (Rx), respectively, with the antenna height to the ground set as 1.25 m. The positions of the Tx and Rx are intentionally set to be closer to the left wall than the right wall to generate propagation paths of different delays reflected by the two walls. A virtual UCA with a radius of 0.5 m and 720 positions is realized at the Tx through the turntable, which rotates clockwise from the 1st position as shown in Fig. 1(a). The distance between the UCA center and the Rx is 6.5 m. Three scenarios are considered in the measurements, i.e., LoS, OLoS1, and OLoS2. In the LoS scenario, the measurement is performed along in an empty room. For the OLoS1 scenario, a metallic board with the length

[1]The ultra-wide bandwidth is defined as either a large relative bandwidth (typically larger than 20% of the center frequency) or a large absolute bandwidth (>500 MHz) [6], [35].

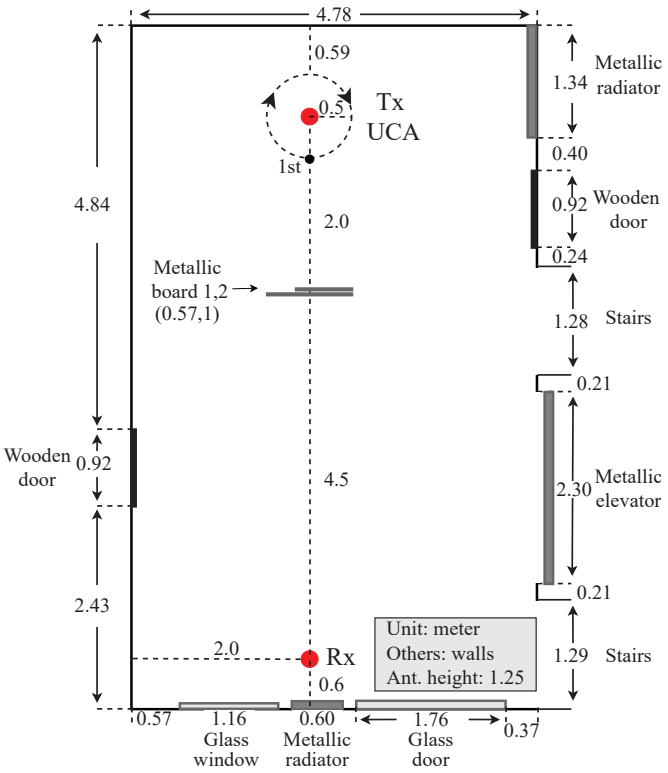

(a)

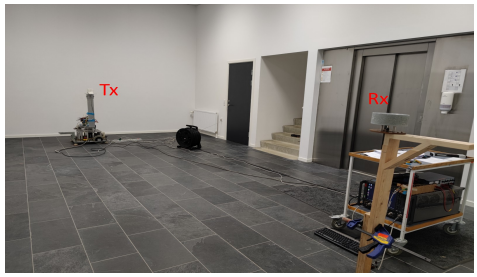

(b)

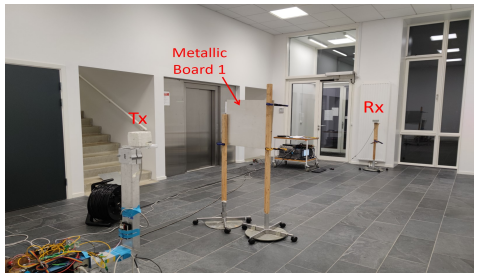

(c)

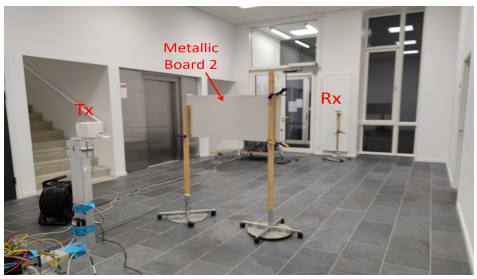

(d)

Fig. 1. The illustration of the measurement room (a) and measurement photographs taken in (b) the LoS scenario, (c) the OLoS1 scenario, and (d) the OLoS2 scenario.

TABLE I
MEASUREMENT SPECIFICATIONS

Parameter	Value
Tx and Rx height	1.25 m
LoS distance	6.5 m
Radius of virtual UCA	0.5 m
Number of array elements	720
Frequency range	26.5-32.5 GHz
Frequency points	1800
Antenna type	Biconical [36] [37]
Polarization	Vertical

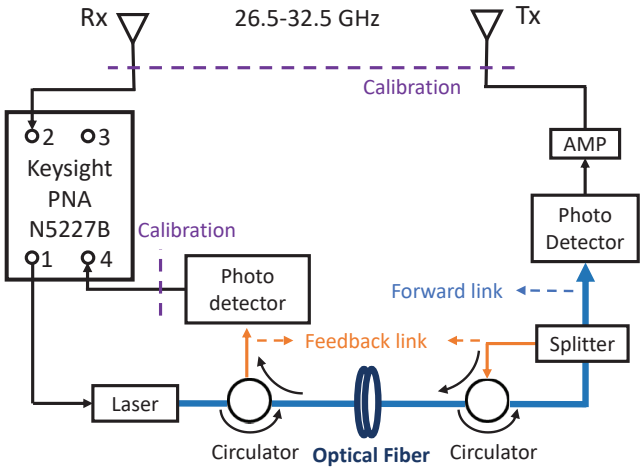

Fig. 2. Block diagram of the measurement system proposed in [38], which consists of a VNA, an amplifier (AMP), and two optical fiber links (forward/feedback). The optical fiber technologies are exploited to prolong the measurement distance and increase the system link budget. The phase change in the optical fiber of the forward link, which arises due to thermal changes and mechanical stress (e.g., cable bending as the turntable rotates for the virtual UCA), would be calibrated out through the feedback link. Calibration between the Tx and Rx would be performed before measurements to de-embed the system response.

of 0.57 m is placed between the transmitter (Tx) UCA and receiver (Rx) to partially obstruct the path in the LoS direction. For the OLoS2 scenario, another 1 m length metallic board was used to completely obstruct the LoS path. Both metallic boards are 0.56 m in width, 2 mm in thickness, and the centers are set at a height of 1.25 m above the ground.

A phase-compensated VNA-based channel measurement system proposed in [38] is utilized to sound the propagation channel, as depicted in Fig. 2. The frequency range from 26.5 to 32.5 GHz is swept with 1800 frequency points for each Tx-Rx pair. That is, for each scenario with the formed virtual UCA, 720 channel frequency responses (CFRs) in sizes of 1800 complex values were collected. The measurement setup enables sounding excess delay up to 300 ns without aliasing, which corresponds to the maximum propagation distance of 90 m. Moreover, the ultra-wide bandwidth of 6 GHz would provide high delay resolution, where multipaths that differ by more than 5 cm in propagation distance would be resolved in the measurements.

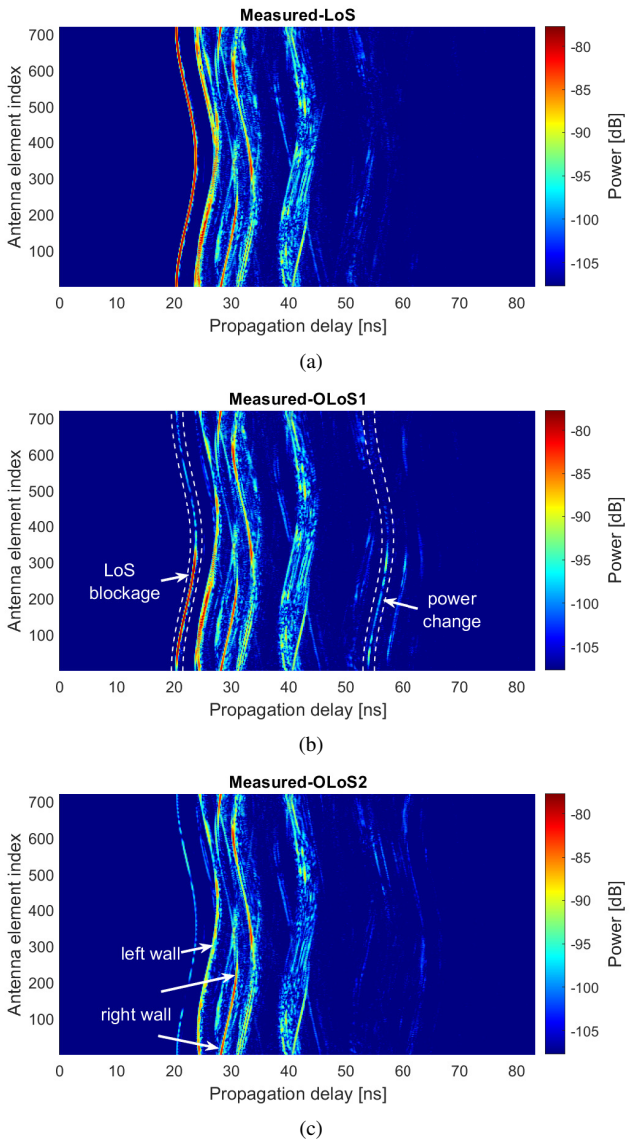

Fig. 3. Measured CIRs across elements in (a) the LoS scenario, (b) the OLoS1 scenario, and (c) the OLoS2 scenario. In the figure, three trajectories are identified and marked as the blocked LoS path, the first-order reflection paths by the left and right walls in the room, respectively. Another path are observed with power change among visible antenna elements. The white dashed lines in (b) mark the trajectory range of the LoS path and power-change path, which help to pick out the two paths for demonstration in Fig. 4.

B. SnS Channel Observations

As mentioned, 720 CFRs are collected in each scenario, represented as $\mathbf{H}_m(f)$ where $m \in [1, 720]$ denotes the antenna element index. After performing inverse discrete Fourier Transform (IDFT), we obtain channel impulse responses (CIRs) $\mathbf{h}_m(\tau)$ across UCA elements. Fig. 3 illustrates measured CIRs in the three scenarios, where the horizontal and vertical axes represent the propagation delay and antenna element index, respectively, and the color denotes the received power (dB). 30 dB[2] of the power dynamic range is set here, as well as in the following discussion of modeling and validation. The

[2]As mmWave systems rely on dominant paths for data transmission, 30 dB is generally considered adequate as the power dynamic range [39].

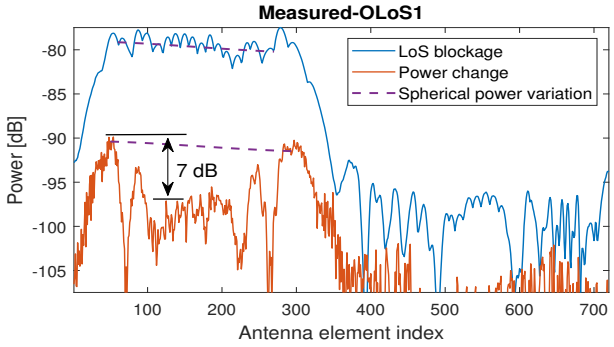

Fig. 4. Power across elements of the blocked LoS path and power-change path, obtained by the white dotted lines in Fig. 3(b). For each path, the spherical power variation across visible elements, which is caused by the distance difference in spherical propagation and calculated according to [42] (also described by (3) in this paper), is illustrated. It can be observed that the spherical-wave model fits the power variation of the LoS path among visible elements well, while failing to capture the power change of around 7 dB on visible elements for the power-change path.

measured channels are observed to be rather sparse with a few dominant paths, though many weak paths are also observed. The mmWave channel sparsity is investigated in detail in [40]. In Fig. 3, channel multipaths can be observed with trajectories like partial or complete s-shaped curves. The shape of those curves represents the delay difference across UCA elements in propagation. It is a result of the distance difference caused by the large array aperture and high delay resolution from the ultra-wide bandwidth. In fact, the propagation characteristics of multipaths can be roughly indicated by the curves. For instance, the curve delays can be averaged to obtain the propagation delay of the multipath, and the propagation angle can be roughly estimated from the delay profile shape per path. By associating the indicated characteristics with the room geometry from ray optics [41], several dominant multipaths can be identified. As marked in Fig. 3, three curves are identified as the blocked LoS path, and the first-order reflection paths from the left and right walls in the measurement room, respectively. Besides, the path trajectory can be picked out with a preset range threshold. An example is shown in Fig. 3(b), where trajectories of the blocked LoS path and the power-change path are picked out by white dashed lines. For each element, the maximal values in the range are detected as the path power. The power results of the picked paths are illustrated in Fig. 4.

The stationarity of the curves across antenna elements, i.e., being complete or partial with/without power change, insinuates the SnS property of multipaths. From observations of Fig. 3 and 4, we have following findings on the SnS characteristic.

- **LoS blockage**. The LoS path trajectory is obstructed partially (in Fig. 3(b)) or completely (in Fig. 3(c)) in the OLoS scenarios, compared to the unblocked one in the LoS scenario (in Fig. 3(a)). It attributes to the presence of the metallic boards in different sizes. Note that the paths with almost same delays but lower power compared to the LoS path in the CIRs come from diffraction on the edges of the metallic boards (same diffracted paths can be observed in Ray-tracing results as shown in Section

IV). As shown in Fig. 4, the LoS path power across unblocked elements basically agree with the calculated spherical power variation. It denotes that after removing the spherical propagation effect, the blocked LoS path is observed with constant power distribution among visible elements. We denote the SnS phenomenon as the LoS blockage.

- **Incomplete reflection**. Besides the LoS path trajectory, we can observe some other incomplete trajectories that have almost constant path power on visible elements. In Fig. 3(c), the left-wall path is observed with a complete trajectory and almost constant power distribution across elements, since the left wall serves as a complete reflection scatterer for the entire array. The right-wall path is observed with an incomplete trajectory and almost constant power distribution, since it is actually reflected by the metallic elevator on the right wall that serves as an incomplete scatterer. We denote the latter phenomenon as incomplete reflection.
- **Power change**. Some paths are observed with incomplete trajectories, where power change among visible elements occurs. An example of power change is marked in Fig. 3(b), and Fig. 4 illustrates the power change of around 7 dB. The power change is not due to the spherical wave propagation, since the latter leads to the power variation at a relatively low level. It is confirmed to be from the diffraction coefficient in Section IV according to the comparison between measured and Ray-tracing results.

The above findings reveal three cases on the SnS characteristic in practical massive MIMO channels: *1)* there still exist stationary multipaths (e.g., the left-wall path) that project almost constant power on all elements of arrays. It results from large-size objects serving as complete reflection scatterers for the entire array. *2)* Due to blockage or incomplete reflection, multipaths might project almost constant power only on part of the array (i.e., visible elements), e.g., the blocked LoS path and the right-wall path. No power will be distributed on the other part (i.e., invisible elements). *3)* Instead of almost constant power distribution, a significant power change among visible elements might occur. It is attributed to the involvement of diffraction in propagation. Especially, the VR-based models, which are state-of-the-art models on SnS as mentioned in Section I, fail to capture and explain the power change since only relatively low spherical power variation among visible elements is assumed. On the contrary, all observed SnS phenomena can be well explained by physical propagation mechanisms as analyzed. Inspired by those findings, a generic, realistic, yet low-complexity channel modeling framework is proposed for massive MIMO antenna systems, where the SnS characteristic is captured from physical propagation mechanism point of view.

III. SnS Channel Modeling Framework

Based on the observations from measurements, a novel SnS propagation channel modeling framework for massive MIMO systems is proposed in this section. Spherical-wave propagation instead of conventional plane-wave assumption is used to characterize near-field channels under the deployment of the large-scale antenna. Besides, a novel parameter is introduced to capture the SnS characteristic, which reveals the observed SnS characteristic from the perspective of multipath propagation mechanisms, i.e., LoS blockage, reflection, diffraction. Finally, the implementation and capabilities of the proposed framework are discussed.

A. Modeling Framework

Let us consider the scenario depicted in Fig. 5 where the base station is equipped with the M-element antenna and the user has a single antenna. Without loss of generality, the same scenario as the measurement is considered here for the sake of consistency, and isotropic antennas and single polarization are assumed for simplicity. As mentioned before, massive MIMO systems might work in the near-field region and hence spherical propagation should be considered. Besides, the SnS characteristic is taken into channel modeling due to the non-stationary observations in the measurements.

We assume there exist K SnS spherical-propagation paths between the Tx array and Rx. The massive MIMO channel at the frequency f can be modeled as a superposition of CFRs of the K paths on the array. It can be succinctly expressed as

$$\mathbf{H}^{\text{sns}}(f) = \mathbf{S} \odot \mathbf{A}(f) \cdot \mathbf{H}(f), \tag{1}$$

where $\mathbf{H}^{\text{sns}}(f)$ comprises M complex values, i.e., $\mathbf{H}^{\text{sns}}(f) \in \mathbb{C}^{M\times 1}$, $f \in [f_L, f_U]$ denotes the frequency within the designed range, and $\odot$ represents element-wise product operation. $\mathbf{H}(f) \in \mathbb{C}^{K\times 1}$ denote CFRs at f of the K paths at the reference point (see Fig. 5),

$$\mathbf{H}(f) = \left[\alpha_1 e^{-j2\pi f\tau_1}, \cdots, \alpha_k e^{-j2\pi f\tau_k}, \cdots, \alpha_K e^{-j2\pi f\tau_K}\right]^T, \tag{2}$$

where $\{\alpha_k, \tau_k\}$ represent complex amplitude and propagation delay of the kth path, respectively. $(\cdot)^T$ denotes the transpose operation. $\mathbf{A}(f) \in \mathbb{C}^{M\times K}$ is the array manifold matrix. The manifold projected on the mth antenna element by the kth path, i.e., $\mathbf{A}$'s (m,k)th entry $a_{m,k}$, can be represented by the transfer difference of the mth element with respect to the reference point, i.e.,

$$a_{m,k}(f) = \frac{\|\boldsymbol{d}_k\|}{\|\boldsymbol{d}_{m,k}\|} e^{-j2\pi f \frac{\|\boldsymbol{d}_{m,k}\| - \|\boldsymbol{d}_k\|}{c}}, \tag{3}$$

where c is the light speed, and $\|\cdot\|$ represents the Euclidean norm of the argument. $\boldsymbol{d}_k$ denotes the vector pointing from the reference point to the first scattering source of the kth path propagation route [42], specifically,

$$\boldsymbol{d}_k = d_k \cdot [\sin\theta_k \cos\phi_k, \sin\theta_k \sin\phi_k, \cos\theta_k]. \tag{4}$$

d_k is the distance between the source and the reference point, and $\{\theta_k, \phi_k\}$ denote the elevation and azimuth angle of the kth path, respectively. $\boldsymbol{d}_{m,k}$ denotes the vector pointing from the mth antenna element to the source point, formalized as

$$\boldsymbol{d}_{m,k} = \boldsymbol{d}_k - \boldsymbol{d}_m, \tag{5}$$

where $\boldsymbol{d}_m$ is the position vector of the mth element with respect to the reference point. Note that the aforementioned

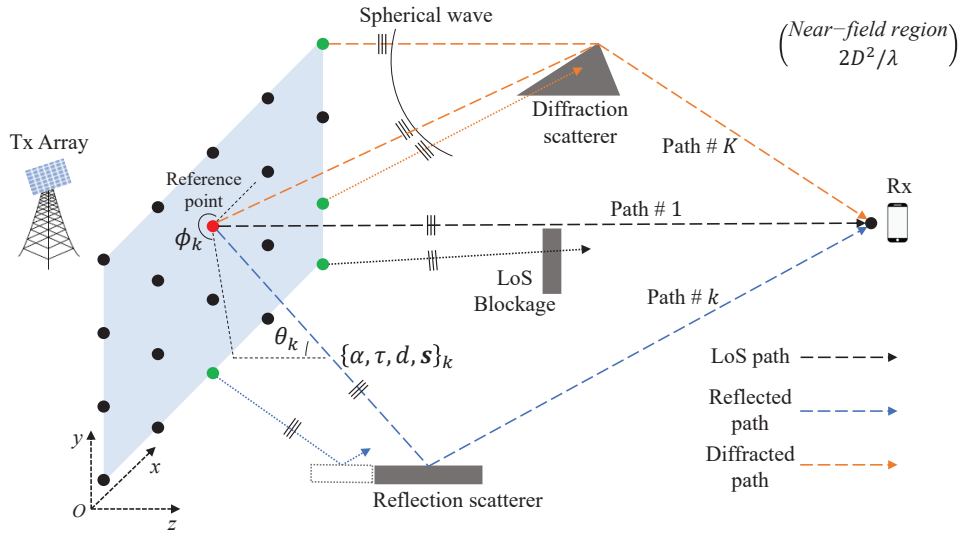

Fig. 5. Spherical propagation with the SnS characteristic. Three cases that contribute to the SnS propagation, i.e., LoS blockage, incomplete reflection, and diffraction, are illustrated.

distance-dependent power variation evenly distributed in the spherical wave [42], is denoted as $\|\boldsymbol{d}_k\| / \|\boldsymbol{d}_{m,k}\|$ in (3).

The SnS characteristic is observed in massive MIMO channels since the objects in the scenario may no longer serve as complete scatterers for the entire antenna array with its aperture increasing. Illustrations are shown in Fig. 5, where different channels are viewed from the elements marked in green and the reference element. We denote VR_k as the VR for the kth path (i.e., elements in VR_k can view the kth path while those out of VR_k can not). In (1), a novel matrix $\mathbf{S}$ is introduced in the proposed modeling framework for the SnS property. It contains K nonnegative real-valued vectors, i.e.,

$$\mathbf{S} = [\boldsymbol{s}_1, \cdots, \boldsymbol{s}_k, \cdots, \boldsymbol{s}_K], \tag{6}$$

where $\boldsymbol{s}_k = [s_{1,k}, \cdots, s_{m,k}, \cdots, s_{M,k}]^T$ and $s_{m,k}$ characterizes the SnS property of the kth path on the mth element. Note that the proposed framework is also applicable of conventional stationary multipaths by setting $s_{m,k} = 1$ for $m = [1, M]$. In principle, $\mathbf{S}$ denotes SnS contributions of propagation paths on the antenna array. For instance, as observed in Fig. 3(c), the two wall-reflected paths propagate with almost constant power on elements in VR_k and no power on elements out of VR_k. It indicates the two SnS paths have same and no contributions on visible and invisible elements, respectively, which can be modeled by setting $s_{m,k} = 1/0$. On the other hand, the observed power change in Fig. 3(b) indicates the necessity of power-varying contributions on elements in VR_k for a diffracted SnS path. To capture the SnS contributions of multipaths, $s_{m,k}$ is specified from the perspective of multipath propagation mechanisms in the following:

- **LoS blockage**. As shown in Fig. 5, the LoS path is partially blocked from the perspective of antenna elements. According to observations in Section II-B, almost constant power is viewed among elements in VR_k and no power among those out of VR_k. Hence, in this case, $s_{m,k}$ is set as 1 and 0 for elements in and out of VR_k, respectively.
- **Reflection**. Multipaths might be reflected on those incomplete scatterers and propagate with the SnS property due to the huge array aperture. As illustrated in the reflection case in Fig. 5, while the reference element can view the kth path, the element marked in green can not due to the limited size of the reflection scatterer. According to measurement results in Section II-B, almost constant power is observed among those elements in VR_k. $s_{m,k}$ is set as 0 and 1 corresponding to $m \notin \mathrm{VR}_k$ and $m \in \mathrm{VR}_k$ in this case, respectively.
- **Diffraction**. Paths whose propagation trajectories are involved by diffraction would propagate with the SnS property. As shown in the diffraction case in Fig. 5, one element marked in green color in the diffraction shadow can not view the diffracted paths, while another one in green and the reference element can. Besides the visible and invisible phenomena, large power change among visible elements would happen. In principle, the diffraction coefficient, which has been widely used to capture diffraction propagation in uniform theory of diffraction (UTD), contributes to the power change [43]–[46] (specifically, see (3) and (5) in [43]). To capture SnS in this case, $s_{m,k}$ is set as 0 for $m \notin \mathrm{VR}_k$ (e.g., the element in shadowing in Fig. 5), and non-negative real values changing with m for $m \in \mathrm{VR}_k$. Fig. 6 presents the UTD theory in a first-order diffraction case, which exemplifies the explanation of the power change phenomenon based on the diffraction mechanism and illustrates the setting of $s_{m,k}$ for this case.
- **Others**. There are penetration and diffused paths in practical propagation. However, these weak paths are ignored in our consideration due to the fact that mmWave systems mainly rely on several dominant paths to transmit data. Besides, diffuse paths usually propagate with broad angle distributions [47], which contribute insignificantly to the SnS characteristic.

As a summary, $s_{m,k}$ is set from the perspective of multipath

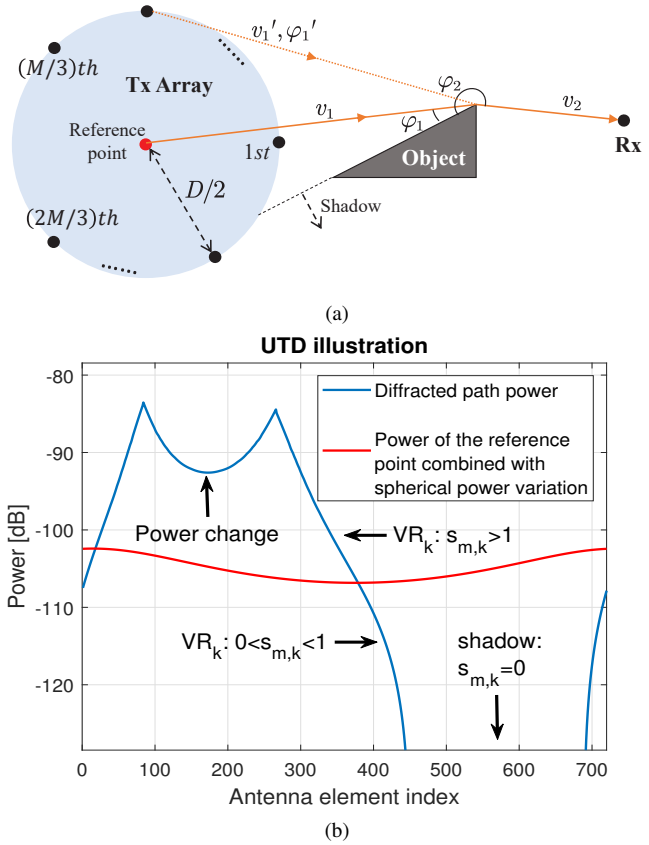

Fig. 6. Illustration of the UTD theory in a first-order diffraction case to explain the observed power change phenomenon. (a) presents the scenario, where a diffracted path is emitted from a Tx UCA to a single-antenna Rx. The parameters are set as the incidence angle $\varphi_1 = 8.5°$, the exit angle $\varphi_2 = 196.8°$, the incidence distance $v_1 = 2$ m, the emit distance $v_2 = 4.5$ m, the element number $M = 720$, and the array aperture $D = 1$ m. The object material is set as metal. (b) presents the diffracted path power across elements, which is calculated according to the UTD theory (specifically, shown in (3) and (5) in [43]). A power change similar to the one in the measurement is observed, demonstrating the SnS phenomenon of the power change can be explained by the diffraction propagation. The $s_{m,k}$ parameter is calculated according to the diffraction coefficient, which actually represents the power ratio between the path power of the array and that of the reference point combined with spherical power variation (related to v_1'/v_1). As shown in (b), the setting of the value range $s_{m,k} \geqslant 0$ can well capture the diffraction case.

propagation mechanisms in the proposed modeling framework, as[3]

$$s_{m,k} \begin{cases} = 0, & m \notin \mathrm{VR}_k \\ = 1, & m \in \mathrm{VR}_k \ \& \ blockage/reflection \\ > 0, & m \in \mathrm{VR}_k \ \& \ diffraction \end{cases} . \quad (7)$$

B. Discussions

Here we present how to generate a realistic SnS channel based on the proposed modeling framework. Fig. 7 presents the implementation of the proposed framework. Assume there exist K multipaths in a massive MIMO SnS channel. For the kth path, the parameter set is given as $\Gamma = \{\alpha, \tau, \theta, \phi, d, \boldsymbol{s}\}$. According to (2) with parameters $\{\alpha, \tau\}$, CFRs of all K paths

[3]Note that the $s_{m,k}$ parameter for the case of the diffraction and $m \in \mathrm{VR}_k$ can be alternatively set with the upper bound, e.g., $0 < s_{m,k} < 1$, by selecting the element with the highest power as the reference.

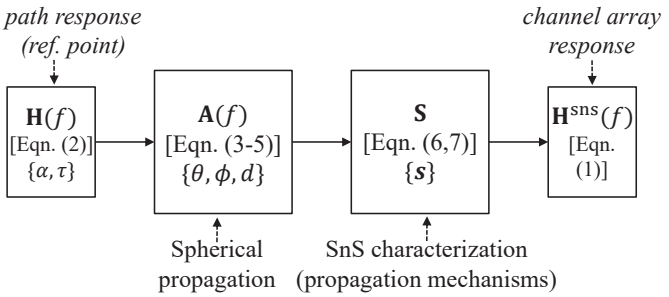

Fig. 7. Implementation of the proposed modeling framework.

at the reference point, i.e., $\mathbf{H}(f)$, can be generated. Then, with spherical wave propagation assumed and knowledge of parameters $\{\theta, \phi, d\}$, the array manifold $\mathbf{A}(f)$ can be realized according to (3)-(5). The path parameter $\boldsymbol{s}$ depicts the SnS characteristic of the path on the array from the perspective of propagation mechanisms. Based on $\boldsymbol{s}$, the matrix $\mathbf{S}$ is introduced in the modeling process and can be obtained through (6) and (7). Finally, the SnS channel can be generated according to (1).

Here we discuss the framework capabilities compared to state-of-the-art works. In the literature on statistical channel models, e.g., [48], spatial stationary near-field channels in massive MIMO systems are usually modeled as

$$\mathbf{H}^{\mathrm{ss}}(f) = \mathbf{A}(f) \cdot \mathbf{H}(f) . \quad (8)$$

Note that it is equivalent to a special case of our proposed framework with setting $s_{m,k} = \mathbf{1}$ for arbitrary m and k. According to (2-5,8), the path parameter set of $\Gamma_{\boldsymbol{s}} = \{\alpha, \tau, \theta, \phi, d\}$ is required in the modeling process. Compared to the spatial stationary channel modeling, only one additional parameter $\boldsymbol{s}$ has been added in the proposed framework to consider SnS. On the other hand, VR-based models, state-of-the-art channel models that consider SnS, fail to properly capture the observed SnS phenomena (e.g., power change as explained). The proposed framework fills the gap by introducing the physical propagation mechanisms, resulting in realistic channel modeling on SnS. Moreover, explanations on SnS from propagation mechanisms are valuable for the flexible implementation of the proposed framework for performance testing (that is, customized SnS channels can be realized flexibly by setting the SnS parameter from propagation mechanisms). In the context of deterministic channel models, such as Ray-tracing [49], realistic SnS channels can be generated due to the site-specific property [24]. However, such models yield a high calculation complexity and require material databases, which makes it less attractive to model SnS for massive MIMO channels using Ray-tracing simulations. To sum up, the proposed framework can generate realistic SnS channels for massive MIMO antenna systems, and its simplicity results in a low-complexity implementation.

IV. Framework Validation

Fig. 8 illustrates the validation strategy. Ray-tracing is used for two reasons: *1)* providing multipath parameters, i.e., Γ,

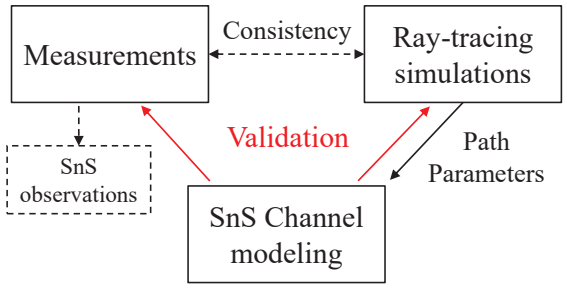

Fig. 8. Strategy of the framework validation. Ray-tracing simulations, which are consistent with the measurements, provide multipath parameters for the proposed modeling framework to regenerate the SnS channels. The validation is carried out by comparing practical SnS channels (i.e., the measurements with the SnS observations and Ray-tracing simulations) with the modeling results.

which are required by the proposed framework for its implementation as mentioned. To the authors' best knowledge, most existing channel parameter estimators fail to work properly in wideband near-field SnS channels [12], [13] since the stationary channel is generally assumed. Hence, it is currently difficult to extract the parameters from the measured data. By contrast, Ray-tracing can generate SnS channels consistent with the measured one, where channel parameters can be obtained directly. *2)* model generalization. The measurement positions are limited due to the high cost of measurements. However, a generic statistical model relies on comprehensive and realistic channel data. Ray-tracing is implemented for more channel data, which can be combined with channel measurements to achieve generalization of the proposed modeling framework. In the validation, Ray-tracing simulations are performed for the target SnS channels (though with high complexity), and the provided parameters can be inputted into the proposed modeling framework. Finally, validation will be performed by comparing the similarity between the target SnS channels (i.e., Ray-tracing simulated channels) and the modeling results. The multipath parameter estimation for ultra-wideband massive MIMO SnS channels and the model generalization can be carried out in the future work.

This section first presents three Ray-tracing simulations corresponding to three measurement scenarios (i.e., LoS, OLoS1, and OLoS2). Then, the validation process is presented. Finally, we discuss the performance of the proposed framework for SnS channel modeling.

A. Ray-tracing Simulations

The commercial Ray-tracing simulator, Wireless InSite [50], is exploited in the simulations. It has been widely used in mmWave research and verified with channel measurement data [51]. As illustrated in Fig. 9, an indoor room with objects is built in the simulator, which is consistent with the measurement room as shown in Fig. 1. Note that the shapes of some objects are slightly adjusted for simplification of the database. For instance, we use cuboids to replace the heating radiators that actually have irregular surfaces in real world. The materials of objects are set according to the International Telecommunication Union (ITU) recommendations [52], including concrete, wood, glass, ceiling board, and metal.

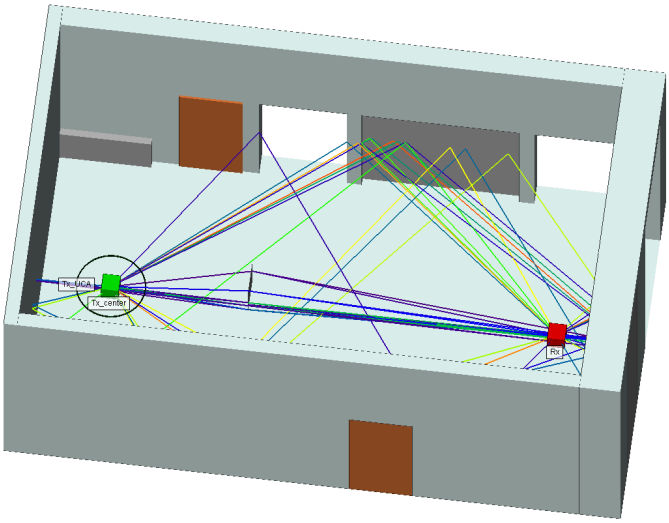

Fig. 9. The Ray-tracing simulation in the OLoS1 scenario with a single antenna equipped at the UCA center as the Tx. The simulation with the 720-element UCA as the Tx is also performed for the target SnS channels. Note that the ceiling board existing in real simulations is invisible here for illustration.

Simulations in three scenarios are performed, i.e., LoS, OLoS1, and OLoS2. In each scenario, two sets of antennas, including a UCA with 720 elements and a single antenna placed at the UCA center, are exploited in the Tx separately. Same as settings in the measurements, omni-directional antennas with vertical polarization are used for all elements. The simulation frequency in Ray-tracing is set as 29.5 GHz and the bandwidth is set as 6 GHz with 1800 frequency samples. The maximum number of propagation path interactions is constrained to be 4 reflections, 1 diffraction, and 1 penetration after consideration of the simulation complexity and accuracy.

B. Validation Process

We exploit the similarity between the target channels (i.e., Ray-tracing results with the UCA) and modeling results for the validation. The operation steps are detailed in the following.

Step 1: generate target SnS channels. For each scenario, the Ray-tracing simulations with the UCA (i.e., 720 antenna elements) as the Tx are performed to obtain the target channels. 720 simulations for all pairs of Tx element-Rx are conduct to generate the realistic SnS spherical-propagation channel, which take around 12 hours for each scenario. We denote the CIR from the target channels as $\mathbf{h}^{\mathrm{tar}}(\tau) \in \mathbb{C}^{720\times 1800}$.

Step 2: generate stationary path responses. For each scenario, the Ray-tracing simulation with a single antenna (at the UCA center) as the Tx is performed to obtain the parameter set $\Gamma_{\bar{\boldsymbol{s}}}$ of multipaths[4]. Based on $\Gamma_{\bar{\boldsymbol{s}}}$, stationary path responses are generated according to (2)-(5) and (8).

Step 3: generate SnS channels. We obtain the SnS parameter $\boldsymbol{s}$ by comparing the stationary path responses and the SnS path responses in Ray-tracing simulations with the UCA.

[4]It might happen that some paths would be seen on UCA elements (i.e., visible elements), yet not on the UCA center due to the large-scale configuration of the UCA. Parameters of those paths are obtained by randomly selecting one visible element in Ray-tracing-UCA simulations.

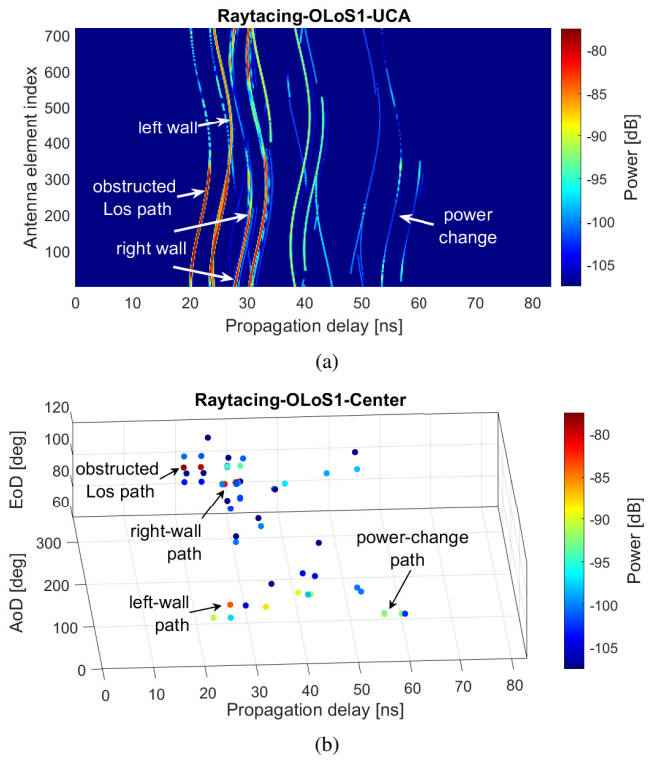

Fig. 10. The Ray-tracing results in the OLoS1 scenario with (a) the UCA and (b) single antenna as the Tx. EoD and AoD in (b) denote elevation and azimuth angle of departure, respectively. Note that additional paths that would be seen on UCA elements yet not on the UCA center (e.g., the LoS path), are included in (b) (see footnote 3). Several multipaths are marked with propagation identifications, corresponding to that in measurement results.

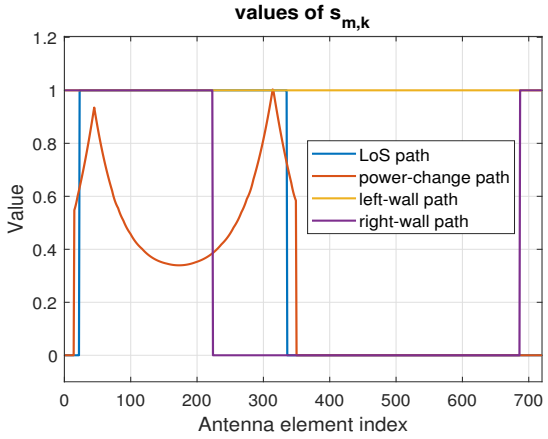

Fig. 11. The $s_{m,k}$ parameter's values of the marked four paths (i.e., the obstructed LoS path, the power-change path, the left-wall path, and the right-wall path) in the OLoS1 scenario, obtained in step 3 of the validation process.

Specifically, for cases of the LoS blockage and reflection, the values would be set as 1/0 for the existence/in-existence of the path response on array elements. For diffraction, non-negative numbers (i.e., $\boldsymbol{s} \geqslant 0$) would be set according to the power change ratio between stationary and SnS path responses. Finally, based on the stationary parameters Γ and the SnS parameter $\boldsymbol{s}$, the SnS CFRs can be modeled according to Section III-B. By applying IDFT, we obtain the SnS CIR $\mathbf{h}^{\mathrm{sns}}(\tau) \in \mathbb{C}^{720\times 1800}$.

Step 4: Similarity calculation. A similarity index between

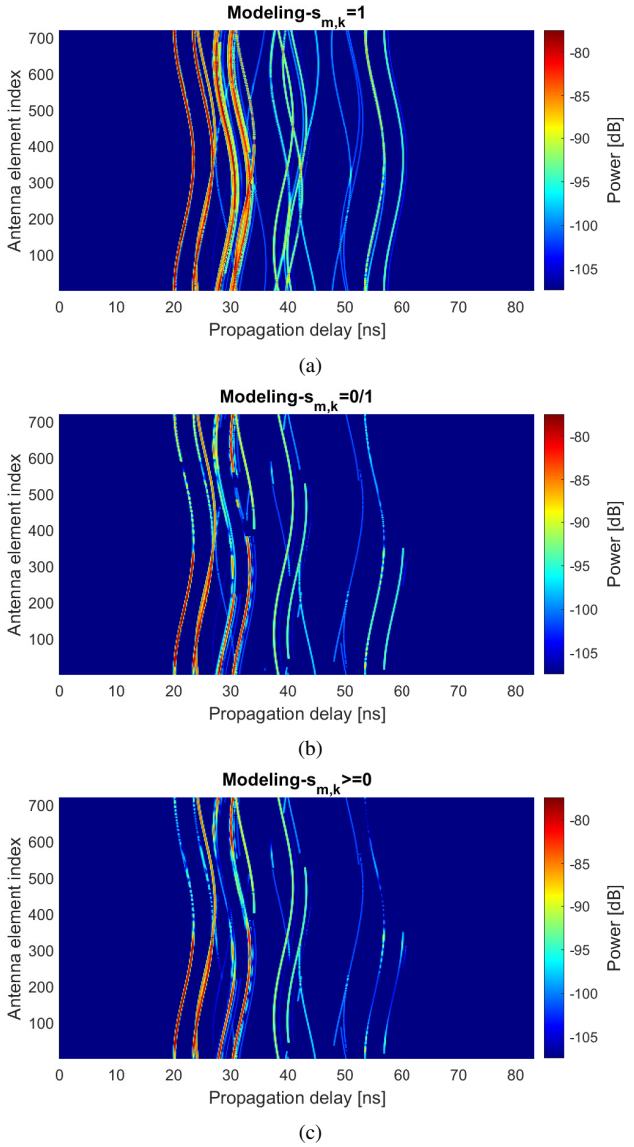

Fig. 12. CIRs across UCA elements in the OLoS1 scenario, obtained by channel realization according to the proposed frameworks. Specifically, (a) denotes the stationary channel modeling result obtained by setting $s_{m,k} = \mathbf{1}$ for arbitrary m and k, corresponding to $\mathbf{H}^{\mathrm{ss}}(f)$ in (8). (b) denotes the SnS channel modeling result with $s_{m,k} = 0/1$, i.e., without consideration of diffraction. (c) represents the complete SnS channel modeling result with $s_{m,k} \geqslant 0$, including the LoS blockage, reflection, and diffraction.

patterns, SI, which has been widely used in MIMO OTA studies [53] and standardized performance testing [54], is utilized to present the similarity between the target channels and the modeling results. It is expressed as

$$SI = 1 - \frac{1}{2}\int \left| \frac{\mathbf{P}^{\mathrm{tar}}(\tau)}{\int \mathbf{P}^{\mathrm{tar}}(\tau)\, d\tau} - \frac{\mathbf{P}^{\mathrm{sns}}(\tau)}{\int \mathbf{P}^{\mathrm{sns}}(\tau)\, d\tau} \right| d\tau. \quad (9)$$

$\mathbf{P}^{\mathrm{tar}}(\tau)$ and $\mathbf{P}^{\mathrm{sns}}(\tau)$ denotes power of CIRs across elements of the target channel and realized channel, respectively, i.e., $\mathbf{P}^{\mathrm{tar}}(\tau) = |\mathbf{h}^{\mathrm{tar}}(\tau)|^2$ and $\mathbf{P}^{\mathrm{sns}}(\tau) = |\mathbf{h}^{\mathrm{sns}}(\tau)|^2$. The range of SI is $[0, 1] \times 100\%$, where 100% denotes full similarity and 0 is maximal dissimilarity.

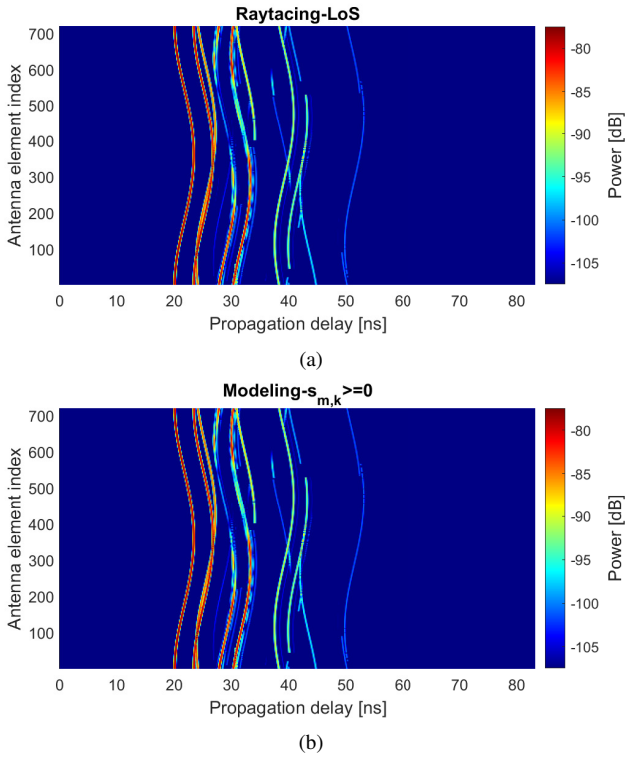

Fig. 13. CIRs across elements in the LoS scenario, obtained by (a) the Ray-tracing simulation with the UCA and (b) channel realization according to the proposed modeling framework.

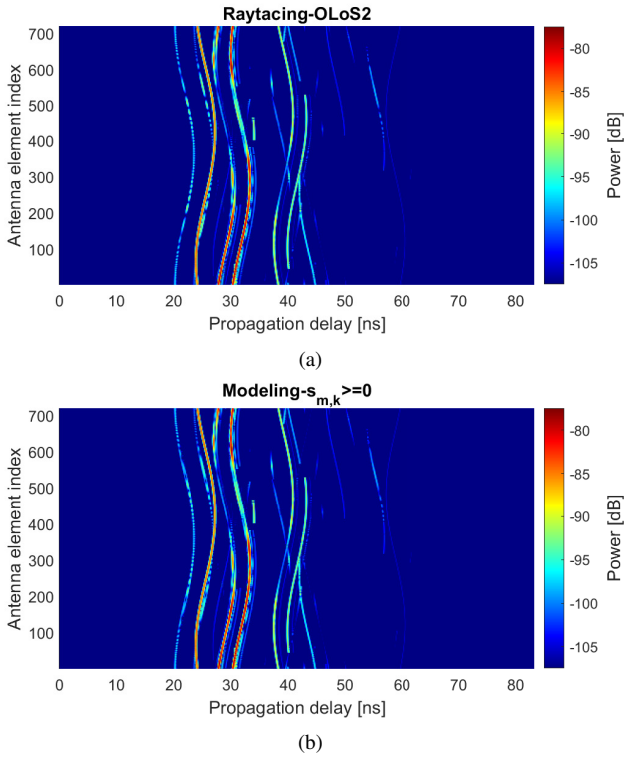

Fig. 14. CIRs across elements in the OLoS2 scenario, obtained by (a) the Ray-tracing simulation with the UCA and (b) channel realization according to the proposed modeling framework.

C. Validation Results

1) OLoS1 Scenario: Fig. 10 illustrates the Ray-tracing results in the OLoS1 scenario. As mentioned before, the result with the UCA employed serves as the target channel for validation, while that with the single antenna at the UCA center provides parameters for channel modeling. We can observe a high similarity between the measured and Ray-tracing-UCA data after comparing Fig. 10(a) with 3(b), where dominant paths in the both results are consistent. The SnS characteristic, which is discovered in measurement results (i.e., LoS blockage, incomplete reflection, and power change), is also clear in the Ray-tracing-UCA result. Note that the power change is found as a result of diffraction with different power distributed on visible elements. Some inconsistencies are also observed. For instance, scattered multipath trajectories with delay as around 40 ns are observed in the measurement, but they disappear in the Ray-tracing result. One main reason is the simplification of objects in simulations as mentioned in Section IV-A (specifically, due to the reconstruction simplification of the radiator near the Rx).

Fig. 11 presents values of the $s_{m,k}$ parameters for several multipaths. Based on the parameters shown in Fig. 10(b) and 11, the SnS channel in the OLoS1 scenario is realized according to the proposed modeling framework, as illustrated in Fig. 12. The stationary channel modeling result, corresponding to (8), is illustrated in Fig. 12(a). All multipaths with the complete trajectories on the array. Compared to the target channel (i.e., Fig. 10(a)), only few stationary paths are modeled well while others are not in this scenario. SI between the stationary modeling result with the target channel is 41.2%. The result presents the significant difference between the stationary model and the realistic SnS channel. It demonstrates the importance of the SnS characteristic in channel modeling. Fig. 12(b) shows the SnS modeling result without consideration of diffraction (i.e., without power change considered). Compared to the target channel, several stationary paths and SnS paths without power change are generated well. It results in SI between them as 89.3%. However, those paths with significant power change observed in the target channel are modeled with almost constant power here. It reveals that the SnS characteristic can not be captured comprehensively only by the concept of VR (i.e., only set elements invisible or visible without power change). The realized channel according to the proposed SnS modeling framework is shown in Fig. 12(c), where all SnS phenomena observed in the measurements are captured well. Moreover, the modeling result is highly similar to the target channel. Besides the stationary paths, all SnS paths that have responses on the partial array with/without power change, are accurately generated. SI between the target and generalized channel is 96.2%[5].

2) LoS and OLoS2 Scenarios: The modeling results in the LoS and OLoS2 scenarios are illustrated in Fig. 13 and 14, respectively. The target channels from Ray-tracing simulations with the UCA are also presented, which show a high similarity to the measured results in Fig. 3. The SnS phenomena ob-

[5]The small deviation between the target and generalized channel (i.e., not achieving 100% similarity) is caused by the approximation error of the used spherical-wave model to the near-field propagation channel [48].

TABLE II
SI BETWEEN TARGET SNS CHANNELS AND MODELING RESULTS

Modeling settings	LoS	OLoS1	OLoS2
Stationary channel-$s_{m,k}=1$	67.7%	41.2%	49.5%
SnS channel-$s_{m,k}=0/1$	95.5%	89.3%	90.0%
SnS channel-$s_{m,k}\geqslant 0$	97.1%	96.2%	94.5%

served in both the measurements and Ray-tracing simulations are captured well in the modeling results. Furthermore, the modeling results match well with the target channels in both scenarios. Specifically, the similarity indexes SIs between them are 97.1%[5] and 94.5%[5] in the LoS and OLoS2 scenarios, respectively.

Table II summaries the performance of channel modeling with different settings in the three scenarios. The high similarity of SI realized by setting $s_{m,k}\geqslant 0$ demonstrates the proposed framework can accurately generate SnS channels in all of the three scenarios. Besides, its implementation for various assumptions (i.e., stationary and SnS assumptions with/without diffraction considered) is flexible, as only one additional parameter is required to be set. Moreover, the proposed framework is low-complexity to use in practice. Specifically, in the validation, the Ray-tracing simulation with 720 antenna elements take about 12 hours to generate realistic SnS channels for each scenario (the used computer is equipped with 1 Intel Xeon E5-2640 CPU, 4 NVIDIA GTX-1080Ti GPUs, and the 128 GB RAM), while the proposed framework generates the channel data within 1 minute on the same computer.

V. CONCLUSION

This paper proposes and validates an SnS massive MIMO channel modeling framework. First, a 6 GHz-bandwidth channel measurement campaign with the large-scale virtual UCA was performed, where realistic SnS phenomena, i.e., existence and in-existence of multipath trajectories in the array axis and significant path power change over visible elements, are clearly observed. Then, based on those observations, we reveal the SnS characteristic from the perspective of multipath propagation mechanisms, i.e., the LoS blockage, reflection, and diffraction. A low-complexity SnS channel modeling framework is proposed with only one additional SnS parameter newly introduced compared to traditional stationary spherical propagation models. Finally, Ray-tracing simulations with the same configurations as the measurements are performed for validating the proposed modeling framework. The SnS phenomena observed in both measured and simulated channels (i.e. LoS blockage, incomplete reflection, and power change), are captured and regenerated well by the proposed framework. The realized channels according to the framework show high similarities to the target Ray-tracing SnS channels, validating its accuracy. Specifically, for the LoS and two OLoS scenarios, the similarity between the target channels and modeling results is calculated as 97.1%, 96.2%, and 94.5% respectively, compared to 67.7%, 41.2%, and 49.5% when only stationary channel is considered. The proposed framework is applicable to realistic SnS channel realization with low complexity, which is desirable for link- and system- level evaluation of massive MIMO antenna systems.

For future work, it would be necessary to propose multipath parameter estimation algorithms for near-field SnS channels. Then we can further characterize the realistic channels for ultra-wideband massive MIMO systems and validate the modeling framework directly with the measured data. Besides, more channel measurements and Ray-tracing simulations will be performed for building a comprehensive massive MIMO channel database, where the generalization of the proposed modeling framework can be realized as discussed. Furthermore, it will be also useful to extend the proposed framework and concept describing the SnS property for the standardized channel models with the cluster structure.

ACKNOWLEDGMENT

The authors would like to thank Yejian Lyu, Mengting Li, and Huaqiang Gao from Aalborg University for assisting the measurements, and thank Fengchun Zhang from Aalborg University for research discussion. The work is supported by the National Science Fund for Distinguished Young Scholars (No. 61925102), the National Key R&D Program of China (No. 2020YFB1805002), the National Natural Science Foundation of China (No. 62031019), BUPT-CMCC Joint Innovation Center, and BUPT Excellent Ph.D. Students Foundation.

REFERENCES

[1] H. Tataria, M. Shafi, A. F. Molisch *et al.*, "6G wireless systems: Vision, requirements, challenges, insights, and opportunities," *Proc. IEEE*, vol. 109, no. 7, pp. 1166–1199, 2021.
[2] E. G. Larsson, O. Edfors, F. Tufvesson *et al.*, "Massive MIMO for next generation wireless systems," *IEEE Commun. Mag.*, vol. 52, no. 2, pp. 186–195, 2014.
[3] J. Zhang, Z. Zheng, Y. Zhang *et al.*, "3D MIMO for 5G NR: Several observations from 32 to massive 256 antennas based on channel measurement," *IEEE Commun. Mag.*, vol. 56, no. 3, pp. 62–70, 2018.
[4] L. Lu, G. Y. Li, A. L. Swindlehurst *et al.*, "An overview of massive MIMO: Benefits and challenges," *IEEE J. Sel. Topics Signal Process.*, vol. 8, no. 5, pp. 742–758, 2014.
[5] F. Rusek, D. Persson, B. K. Lau *et al.*, "Scaling up MIMO: Opportunities and challenges with very large arrays," *IEEE Signal Process. Mag.*, vol. 30, no. 1, pp. 40–60, 2013.
[6] A. F. Molisch, D. Cassioli, C.-C. Chong *et al.*, "A comprehensive standardized model for ultrawideband propagation channels," *IEEE Trans. Antennas Propag.*, vol. 54, no. 11, pp. 3151–3166, 2006.
[7] J. Zhang, Y. Zhang, Y. Yu *et al.*, "3-D MIMO: How much does it meet our expectations observed from channel measurements?" *IEEE J. Sel. Areas Commun.*, vol. 35, no. 8, pp. 1887–1903, 2017.
[8] T. S. Rappaport, Y. Xing, G. R. MacCartney *et al.*, "Overview of millimeter wave communications for fifth-generation 5G wireless networks—with a focus on propagation models," *IEEE Trans. Antennas Propag.*, vol. 65, no. 12, pp. 6213–6230, 2017.
[9] W. Fan, I. Carton, P. Kyosti *et al.*, "A step toward 5G in 2020: Low-cost OTA performance evaluation of massive MIMO base stations." *IEEE Antennas Propag. Mag.*, vol. 59, no. 1, pp. 38–47, 2017.
[10] S. Payami and F. Tufvesson, "Channel measurements and analysis for very large array systems at 2.6 GHz," in *6th EuCAP*, 2012, pp. 433–437.
[11] X. Gao, F. Tufvesson, O. Edfors *et al.*, "Measured propagation characteristics for very-large MIMO at 2.6 GHz," in *IEEE ASILOMAR*, 2012, pp. 295–299.
[12] F. Zhang and W. Fan, "Near-field ultra-wideband mmwave channel characterization using successive cancellation beamspace UCA algorithm," *IEEE Trans. Veh. Technol.*, vol. 68, no. 8, pp. 7248–7259, 2019.
[13] X. Cai, W. Fan, X. Yin *et al.*, "Trajectory-aided maximum-likelihood algorithm for channel parameter estimation in ultrawideband large-scale arrays," *IEEE Trans. Antennas Propag.*, vol. 68, no. 10, pp. 7131–7143, 2020.

[14] J. Li, B. Ai, R. He *et al.*, "The 3D spatial non-stationarity and spherical wavefront in massive MIMO channel measurement," in *IEEE 10th WCSP*, 2018, pp. 1–6.

[15] Q. Wang, B. Ai, D. W. Matolak *et al.*, "Spatial variation analysis for measured indoor massive MIMO channels," *IEEE Access*, vol. 5, pp. 20 828–20 840, 2017.

[16] J. Li, B. Ai, R. He *et al.*, "On 3D cluster-based channel modeling for large-scale array communications," *IEEE Trans. Wireless Commun.*, vol. 18, no. 10, pp. 4902–4914, 2019.

[17] J. Huang, R. Feng, J. Sun *et al.*, "Multi-frequency millimeter wave massive MIMO channel measurements and analysis," in *IEEE ICC*, 2017, pp. 1–6.

[18] C. Wang, J. Zhang, L. Tian *et al.*, "The spatial evolution of clusters in massive MIMO mobile measurement at 3.5 GHz," in *IEEE 85th VTC*, 2017, pp. 1–6.

[19] S. R. Saunders and A. Aragón-Zavala, *Antennas and propagation for wireless communication systems*. John Wiley & Sons, 2007.

[20] B. Ai, K. Guan, R. He *et al.*, "On indoor millimeter wave massive MIMO channels: Measurement and simulation," *IEEE J. Sel. Areas Commun.*, vol. 35, no. 7, pp. 1678–1690, 2017.

[21] J. Zhang, P. Tang, L. Yu *et al.*, "Channel measurements and models for 6G: current status and future outlook," *Frontiers of information technology & electronic engineering*, vol. 21, no. 1, pp. 39–61, 2020.

[22] "Study on channel model for frequencies from 0.5 to 100 GHz," 3GPP, Rep. TR 38.901 V14.0.0, Mar. 2017.

[23] P. Zhang, J. Chen, X. Yang *et al.*, "Recent research on massive MIMO propagation channels: A survey," *IEEE Commun. Mag.*, vol. 56, no. 12, pp. 22–29, 2018.

[24] "METIS channel models," document Deliverable/ICT-317669/D1.4 V3, Tech. Rep., Mar. 2017.

[25] L. Liu, C. Oestges, J. Poutanen *et al.*, "The COST 2100 MIMO channel model," *IEEE Wireless Commun.*, vol. 19, no. 6, pp. 92–99, 2012.

[26] X. Gao, F. Tufvesson, and O. Edfors, "Massive MIMO channels — measurements and models," in *IEEE ASILOMAR*, 2013, pp. 280–284.

[27] S. Wu, C.-X. Wang, H. Haas *et al.*, "A non-stationary wideband channel model for massive MIMO communication systems," *IEEE Trans. Wireless Commun.*, vol. 14, no. 3, pp. 1434–1446, 2015.

[28] C. F. López and C.-X. Wang, "Novel 3-D non-stationary wideband models for massive MIMO channels," *IEEE Trans. Wireless Commun.*, vol. 17, no. 5, pp. 2893–2905, 2018.

[29] E. T. Michailidis, N. Nomikos, P. Trakadas *et al.*, "Three-dimensional modeling of mmwave doubly massive MIMO aerial fading channels," *IEEE Trans. Veh. Technol.*, vol. 69, no. 2, pp. 1190–1202, 2020.

[30] R. He, O. Renaudin, V.-M. Kolmonen *et al.*, "Characterization of quasi-stationarity regions for vehicle-to-vehicle radio channels," *IEEE Trans. Antennas Propag.*, vol. 63, no. 5, pp. 2237–2251, 2015.

[31] J. Li, B. Ai, R. He *et al.*, "A cluster-based channel model for massive MIMO communications in indoor hotspot scenarios," *IEEE Trans. Wireless Commun.*, vol. 18, no. 8, pp. 3856–3870, 2019.

[32] M. Zhu, G. Eriksson, and F. Tufvesson, "The COST 2100 channel model: Parameterization and validation based on outdoor MIMO measurements at 300 MHz," *IEEE Trans. Wireless Commun.*, vol. 12, no. 2, pp. 888–897, 2013.

[33] J. Flordelis, X. Li, O. Edfors *et al.*, "Massive MIMO extensions to the COST 2100 channel model: Modeling and validation," *IEEE Trans. Wireless Commun.*, vol. 19, no. 1, pp. 380–394, 2020.

[34] C.-X. Wang, S. Wu, L. Bai *et al.*, "Recent advances and future challenges for massive MIMO channel measurements and models," *Sci. China Inf. Sci.*, vol. 59, no. 2, pp. 1–16, 2016.

[35] A. Molisch, "Ultrawideband propagation channels-theory, measurement, and modeling," *IEEE Trans. Veh. Technol.*, vol. 54, no. 5, pp. 1528–1545, 2005.

[36] S. S. Zhekov, A. Tatomirescu, and G. F. Pedersen, "Antenna for ultrawideband channel sounding," *IEEE Antennas Wireless Propag. Lett.*, vol. 16, pp. 692–695, 2017.

[37] W. Fan, I. Carton, J. Ø. Nielsen *et al.*, "Measured wideband characteristics of indoor channels at centimetric and millimetric bands," *EURASIP Journal on Wireless Communications and Networking*, vol. 2016, no. 1, pp. 1–13, 2016.

[38] A. W. Mbugua, W. Fan, K. Olesen *et al.*, "Phase-compensated optical fiber-based ultrawideband channel sounder," *IEEE Trans. Microwave Theory Tech.*, vol. 68, no. 2, pp. 636–647, 2020.

[39] M. K. Samimi and T. S. Rappaport, "3-D millimeter-wave statistical channel model for 5G wireless system design," *IEEE Trans. Microwave Theory Tech.*, vol. 64, no. 7, pp. 2207–2225, 2016.

[40] R. He, B. Ai, G. Wang *et al.*, "Wireless channel sparsity: Measurement, analysis, and exploitation in estimation," *IEEE Wireless Commun.*, vol. 28, no. 4, pp. 113–119, 2021.

[41] F. Zhang, W. Fan, and G. F. Pedersen, "Frequency-invariant uniform circular array for wideband mm-wave channel characterization," *IEEE Antennas Wireless Propag. Lett.*, vol. 16, pp. 641–644, 2017.

[42] X. Yin, S. Wang, N. Zhang *et al.*, "Scatterer localization using large-scale antenna arrays based on a spherical wave-front parametric model," *IEEE Trans. Wireless Commun.*, vol. 16, no. 10, pp. 6543–6556, 2017.

[43] R. Luebbers, "Finite conductivity uniform GTD versus knife edge diffraction in prediction of propagation path loss," *IEEE Trans. Antennas Propag.*, vol. 32, no. 1, pp. 70–76, 1984.

[44] A. Kanatas, I. Kountouris, G. Kostaras *et al.*, "A UTD propagation model in urban microcellular environments," *IEEE Trans. Veh. Technol.*, vol. 46, no. 1, pp. 185–193, 1997.

[45] W. Burnside and K. Burgener, "High frequency scattering by a thin lossless dielectric slab," *IEEE Trans. Antennas Propag.*, vol. 31, no. 1, pp. 104–110, 1983.

[46] F. Hacıvelioğlu, M. Alper Uslu, and L. Sevgi, "A matlab-based virtual tool for the electromagnetic wave scattering from a perfectly reflecting wedge," *IEEE Antennas Propag. Mag.*, vol. 53, no. 6, pp. 234–243, 2011.

[47] V. Degli-Esposti, F. Fuschini, E. M. Vitucci *et al.*, "Measurement and modelling of scattering from buildings," *IEEE Trans. Antennas Propag.*, vol. 55, no. 1, pp. 143–153, 2007.

[48] K. Haneda, J.-I. Takada, and T. Kobayashi, "A parametric UWB propagation channel estimation and its performance validation in an anechoic chamber," *IEEE Trans. Microwave Theory Tech.*, vol. 54, no. 4, pp. 1802–1811, 2006.

[49] F. Fuschini, M. Zoli, E. M. Vitucci *et al.*, "A study on millimeter-wave multiuser directional beamforming based on measurements and ray tracing simulations," *IEEE Trans. Antennas Propag.*, vol. 67, no. 4, pp. 2633–2644, 2019.

[50] Remcom, "Wireless insite." [Online]. Available: https://www.remcom.com/wireless-insite.

[51] V. Va, J. Choi, T. Shimizu *et al.*, "Inverse multipath fingerprinting for millimeter wave V2I beam alignment," *IEEE Trans. Veh. Technol.*, vol. 67, no. 5, pp. 4042–4058, 2018.

[52] "Effects of building materials and structures on radiowave propagation above about 100 MHz," Recommendation ITU-R P.2040-1, Tech. Rep., Jul. 2015.

[53] P. Kyösti, L. Hentilä, W. Fan *et al.*, "On radiated performance evaluation of massive MIMO devices in multiprobe anechoic chamber OTA setups," *IEEE Trans. Antennas Propag.*, vol. 66, no. 10, pp. 5485–5497, 2018.

[54] H. Gao, Z. Wang, X. Zhang *et al.*, "Over-the-air performance testing of 5G new radio user equipment: Standardization and challenges," *IEEE Communications Standards Magazine*, 2022.